



# Femtosecond laser-induced breakdown spectroscopy for film analysis of cu-coated polymer textiles

Omar Elsheikh<sup>1,2</sup> · Bastian Zielinski<sup>1,2</sup> · Noemí Aguiló-Aguayo<sup>3</sup> · Elena Ramela Ciobotea<sup>2</sup> · Cristian Sarpe<sup>2</sup> · Hendrike Braun<sup>2</sup> · Arne Senftleben<sup>2</sup> · Thomas Baumert<sup>2</sup> · Camilo Florian<sup>1,2</sup>

Received: 28 August 2025 / Accepted: 13 January 2026  
© The Author(s) 2026

## Abstract

The objective of this work is to evaluate the capability of femtosecond laser-induced breakdown spectroscopy (fs-LIBS) to characterize copper coatings on Lyocell textile fibers with micrometric spatial resolution. In this study, fs-LIBS is employed as a high-resolution analytical technique for characterizing copper coatings on heat-sensitive polymer-based Lyocell fabric. A relative spectral analysis of the multilayered material was performed by tracking relative variations in emission lines within the coating thickness and in spatially selected regions where the coloring is inhomogeneous. The observed color inhomogeneity arises from local variations in oxide formation and particle density during the copper deposition process. A coated textile sample was inspected via scanning electron microscopy (SEM) and Energy-dispersive X-ray spectroscopy (EDX) from the surface to the polymer substrate to estimate a Cu coating thickness of approximately 20  $\mu\text{m}$  and fiber diameters of approximately 175  $\mu\text{m}$ . SEM-EDX was used only to estimate coating thickness, as its limited sensitivity to light elements and buried interfaces makes it unsuitable for resolving the polymer and oxide signatures targeted in this work. The proposed measuring approach based on fs-LIBS enabled precise chemical mapping with a lateral resolution of 7  $\mu\text{m}$  linked to the implemented focusing optics and shallow depth profiling with minimal thermal damage to the underlying polymer substrates. The technique successfully identified key elements such as Copper (Cu-I) and trace contaminants such as Silver (Ag-I), Tin (Sn-II), and Sodium (Na-I), introduced during silver seeding and electroless copper deposition. Additionally, due to the ultrashort pulse duration of the laser pulses used, CN and C–C band spectral lines coming from the dielectric polymer, as well as Cu oxides (CuO, Cu<sub>2</sub>O) originating from extremely thin surface layers, could also be detected. These findings highlight the capability of fs-LIBS for spatially selective, minimally invasive, real-time analysis and demonstrate its compatibility with the characterization of thin films deposited on thermally sensitive substrates, relevant for flexible electronics and smart textile applications.

**Keywords** Femtosecond laser induced breakdown spectroscopy · fs-LIBS · Copper coated textiles · Flexible electronics · Chemical mapping

## 1 Introduction

Flexible electronics are recognized for their unique properties, such as lightweight, deformability, and adaptability, which make them suitable for wearable devices and energy harvesting applications. For instance, flexible polymer-based substrates are critical for ensuring performance in terms of durability and reliability in wearable electronics, as highlighted in reviews discussing their role in flexible displays, implantable sensors, and energy storage systems [1]. Wearable electronics, including smartwatches and health monitoring devices, benefit from the integration of flexible materials such as carbon nanotubes and graphene,

---

✉ Camilo Florian  
camilo.florian@uni-kassel.de

<sup>1</sup> Institute of Materials Engineering, University of Kassel, Mönchebergstraße. 3, 34125 Kassel, Germany

<sup>2</sup> Institute of Physics, University of Kassel, Heinrich-Plett-Str. 40, 34132 Kassel, Germany

<sup>3</sup> Research Institute of Textile Chemistry and Textile Physics, University of Innsbruck, Hoehsterstrasse 73, 6850 Dornbirn, Austria

which offer high electrical conductivity and structural flexibility [2]. Additionally, flexible energy harvesters, such as piezoelectric and triboelectric devices, are increasingly used for self-powered wearable systems, enabling sustainable energy solutions for portable devices [3]. Textile-based energy storage solutions, such as textile batteries, are also gaining attention for their ability to conform to various shapes and provide lightweight, wearable power sources. These advancements are crucial for enhancing comfort and functionality in smart textiles [4].

One widespread laser-based technique that enables rapid elemental analysis, especially for metal-based materials, is laser-induced breakdown spectroscopy (LIBS) [5]. Typical commercial instruments employ nanosecond laser pulses to generate a plasma spark that is subsequently analyzed with a spectrometer. Analyzing metal coatings in textile dyes using nanosecond laser-induced breakdown spectroscopy (ns-LIBS) has gained traction due to its ability to analyze various elements with minimal sample preparation. While ns-LIBS is effective at detecting metals such as copper, magnesium, and manganese in complex matrices such as aluminum alloys, highlighting its suitability for rapid elemental analysis [6, 7], the longer pulse duration leads to stronger laser–plasma interaction and heat diffusion into the material, which can introduce thermal effects that are undesirable for heat-sensitive substrates such as superficial oxides and polymers. In addition, nanosecond pulses can interact with the expanding plasma plume, a process known as plasma shielding, which reduces the amount of laser energy reaching the surface and modifies the ablation efficiency [8]. At the same time, recent studies have demonstrated that optimized ns- $\mu$ LIBS systems can achieve excellent sensitivity, repeatability, and high-quality elemental imaging [9, 10].

In contrast, femtosecond laser-induced breakdown spectroscopy (fs-LIBS) offers several advantages, including the possibility to produce ablation at lower pulse energies and higher spatial resolution thanks to the smaller heat-affected zone, which enhances the analytical performance [11–13]. For ablation, ultra-short pulse duration of femtosecond lasers allows for more efficient interaction with the electron subsystem of dielectric material, leading to improved signal-to-noise ratios and reduced interference from ambient gases [14]. Additionally, fs laser pulses allow minimizing thermal effects and enhancing the detection of trace elements, which is crucial for analyzing complex dye matrices. The rapid ablation process in fs-LIBS results in a more controlled plasma environment, and when combined with a timely spectra recording process, it allows for better differentiation of elemental emissions and improved analytical accuracy that also includes information from dielectric materials and molecular vibrational modes [15]. In this context, the choice of fs-LIBS in the present study is motivated

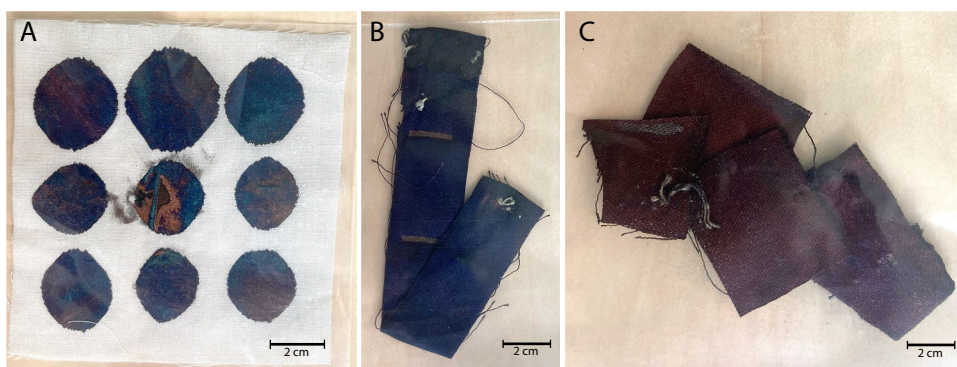
primarily by its negligible thermal load and high spatial precision, which are essential for probing thin metallic layers on heat-sensitive textile fibers.

These general advantages have been demonstrated in various fs-LIBS applications, including high-resolution elemental imaging of thin films and microstructured surfaces, quantitative depth profiling, and chemical imaging with micrometer-scale spatial resolution. Ahamer et al. used fs-LIBS for elemental imaging of thin films, achieving lateral resolutions on the order of a few micrometers [16]. Giannakaris et al. reported single-pulse and orthogonal double-pulse fs-LIBS with femtogram mass detection and chemical imaging at micrometer spatial resolution, highlighting the potential of fs excitation for highly localized analysis [17]. Sheta et al. showed that femtosecond laser-induced plasmas can exhibit enhanced repeatability compared to longer-pulse excitation, emphasizing improved signal stability for analytical purposes [18]. More recently, Saha et al. demonstrated the analytical potential of fs-LIBS for trace-element determination in speleothems, illustrating that fs-LIBS can provide sensitive, depth-resolved information in chemically and structurally complex matrices [19].

Traditional surface characterization techniques, including energy-dispersive X-ray spectroscopy (EDX), X-ray photoelectron spectroscopy (XPS), and secondary ion mass spectrometry (SIMS), exhibit notable limitations when analyzing metallic coatings on flexible substrates. EDX provides elemental mapping but lacks molecular specificity and often requires sample preparation that can alter the substrate's properties, particularly textiles [20]. Standard XPS, while surface-sensitive, demands ultra-high vacuum conditions and suffers from low lateral resolution, which restricts its applicability for detailed surface analysis [21]. SIMS, despite its molecular sensitivity, is less suited for soft, porous materials, posing challenges for substrates with complex morphologies [22]. In contrast, fs-LIBS offers high spatial resolution, depth profiling capabilities, minimal sample thermal damage, and the capacity to work under environmental conditions, making it ideal for analyzing heat-sensitive substrates such as Lyocell. Its minimal sample preparation and high sensitivity for surface composition further enhance its suitability for textile applications.

The production of copper-coated fabric (Cu-coated), involving silver seeding and contactless electroplating has been demonstrated by different studies on advanced coating techniques for textiles [23, 24]. The chemical composition of the finally deposited material can be modified with processing parameters such as deposition time and current density, which play critical roles in coating performance optimization [25]. In this context, fs-LIBS provides an appropriate analytical tool to characterize such coatings due to its capacity to probe metallic and dielectric layers

**Fig. 1** Photographs of Cu-coated Lyocell fabric under white fluorescent ambient light, (A) inhomogeneous coloring including green, orange and yellow regions, (B) homogeneous blue strip, and (C) homogeneous purple strips



with minimal thermal impact. These variations in deposition conditions also lead to the observed color differences (blue, purple, brown), which arise from changes in copper layer thickness, oxidation state, and nanoparticle density formed during the electroless deposition process.

## 2 Sample preparation and experimental setup

This study utilized Cu-coated Lyocell fabric samples, prepared through a two-step process involving silver seeding followed by electroless copper deposition [24]. The samples used in the experiments are all presented in Fig. 1, including blue, purple and brown Cu-coated Lyocell fabric. The seeding process began with padding prewashed fabrics using an aqueous  $\text{AgNO}_3$  solution (5.8 mM, 14.7 mM, or 29.4 mM) at a nip pressure of 2 bar and a roller speed of 2 m/min, followed by drying in ambient atmosphere to ensure uniform silver nanoparticle distribution. Subsequently, the silver-seeded samples were immersed and stirred in a solution containing  $7 \text{ gL}^{-1} \text{ CuSO}_4$ ,  $2.01 \text{ gL}^{-1} \text{ NaCO}_3$ ,  $12 \text{ gL}^{-1} \text{ C}_4\text{H}_5\text{KO}_6$ , and  $10 \text{ gL}^{-1} \text{ NaOH}$  in deionized water, with copper reduction initiated by adding  $26 \text{ mL}^{-1} \text{ H}_2\text{CO}$ . To enhance copper content and achieve varying coating thicknesses, deposition times were extended from 40 min to 2 hours, resulting in samples with distinct color variations and structural integrity preserved for subsequent fs-LIBS analysis.

The experimental setup for fs-LIBS in Fig. 2 utilized laser pulses with a temporal width of 30 fs at a central wavelength of 790 nm and a repetition rate of 1 kHz, generated by an amplified Ti:Sapphire (Ti:Sa) laser system (Femto-lasers, Femtopower Pro). The repetition rate was reduced to single-shot mode using a Pockels cell within the amplifier as an electro-optic pulse selector, ensuring precise pulse control. Linearly polarized light was directed through a high-precision, home-built pulse shaper used to pre-compensate dispersion introduced by optical elements in the beam path, such as the microscope objective, to ensure a

30 fs pulse width at the sample. Pulse length was measured by autocorrelation performed with the same system [26]. The emitted pulses exhibit a near-Gaussian temporal profile typical of Ti:Sa chirped-pulse-amplified systems, and the spatial energy distribution at focus follows a Gaussian

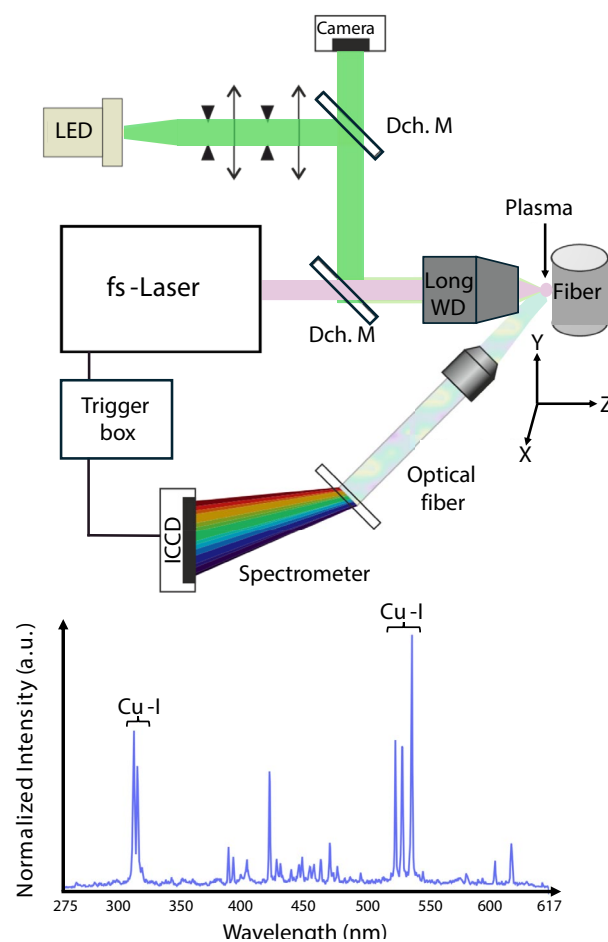


**Fig. 2** The fs laser is focused onto the sample surface to generate a micro-plasma, while an in-situ illumination path enables real-time imaging of the analysis spot. Plasma emission is collected by an objective lens and coupled into an optical fiber connected to the spectrometer and gated ICCD detector. A simplified representation of the resulting spectrum is shown for illustration. All fs-LIBS measurements were performed directly in ambient air without gas confinement

beam profile, consistent with the measured  $1/e^2$  beam waist. The microscope platform was equipped with a monitoring camera for sample positioning, a stepper-motor-controlled XYZ translation stage (PI miCos) with  $1\ \mu\text{m}$  lateral and axial resolution, and a tilt stage to align the sample surface parallel to the stage X and Y axis. A  $10\times$  Mitutoyo Plan Apo objective (numerical aperture  $\text{NA} = 0.28$ , working distance  $\text{WD} = 34\ \text{mm}$ ) focused the pulses to a measured beam waist of  $3.5\ \mu\text{m}$  (at  $1/e^2$  intensity), creating a light-emitting plasma on the sample that was collected by an objective lens positioned at  $45^\circ$  close to the microscope objective. In all experiments, the laser beam was focused such that the focal plane coincided with the sample surface. This was achieved by maximizing the plasma brightness on the monitoring camera while maintaining the smallest achievable spot size on the textile fiber. The surface-focus condition was used consistently for both surface measurements and for initiating depth profiling.

The plasma emission was coupled into a multimode optical fiber bundle (Thorlabs BFL105HS02) consisting of seven fibers, each with a core diameter of  $105\ \mu\text{m}$ . The bundle features a round fiber arrangement on the collection side and a linear arrangement on the spectrometer input side, ensuring efficient light collection and uniform coupling into the spectrograph entrance slit. The fibers have a numerical aperture (NA) of  $0.22 (\pm 0.02)$ , matched to the NA of the fused silica collection optics used in the setup. The multimode configuration enhances signal throughput while maintaining stable coupling for the relatively weak fs-LIBS plasma emission.

The collected emission was analyzed using a LOT–Oriol Multispec MS125 imaging spectrometer equipped with a 400 lines/mm grating featuring a 500 nm blaze wavelength. Prior to all measurements, the wavelength axis of the LOT–Oriol Multispec MS125 spectrometer coupled to the PI-MAX ICCD was calibrated using an L.O.T. Oriol Pen-Ray 6035 Hg(Ar) lamp. This procedure ensured accurate peak-position determination across the entire 275–617 nm spectral range. Under the configuration used in this work, the spectrometer provided a spectral resolution of approximately 1 nm, determined from calibration line widths. Although this resolution does not resolve closely spaced lines, it is sufficient for distinguishing the main Cu-I, Sn-II, Ag-I, Na-I, and CN/C-C features investigated in this study. The dispersed light was recorded over 1024 detector pixels, covering the wavelength range 275–617 nm used in this study. Detection was performed with a Roper Scientific PI-MAX ICCD camera, operated with a gate delay of 85 ns and gate width of 500 ns relative to the laser pulse to suppress continuum emission while maintaining strong atomic and molecular line visibility. Under these gating conditions,

the early-time Bremsstrahlung continuum is strongly suppressed, and the remaining continuous background becomes negligible compared to the discrete emission lines, so no additional spectral correction for continuum emission was required. This configuration ensured optimal sensitivity for the detection of Cu emission lines, trace elements (Ag, Sn, Na), and polymer-related molecular bands [12].

Initially, recorded spectra from irradiation experiments were conducted using single pulses with various energies per pulse (1 to  $8\ \mu\text{J}$ ), as depicted in Fig. 3(A). Each spectra showcases peaks with different intensities that will be later compared with a signature database for the identification of different chemical elements. Additionally, the spectra is used to find the pulse energy where the best signal-to-noise ratio (SNR) is recorded while preserving the integrity of the Cu-coating, as plotted in Fig. 3(B). Lower pulse energies (e.g., 1 to  $3\ \mu\text{J}$ ) exhibited a reduced peak signal, with increased noise compared to higher energies. Optimal SNR was achieved starting at  $4\ \mu\text{J}$ , and therefore, for the subsequent experiments, the pulse energy of  $5\ \mu\text{J}$  and  $6\ \mu\text{J}$  was chosen. The signal-to-noise ratio (SNR) was calculated as the ratio between the peak intensity of the most intense Cu I emission line and the standard deviation of the background signal evaluated in a line-free spectral window. The data included in Fig. 3(A) was normalized using the min-max normalization method to scale the intensity values between 0 and 1. Each spectrum corresponds to the average data collected from 25 laser spots, with the peaks representing emission intensities at various wavelengths ranging from 275 to 617 nm.

A more detailed optical profilometer micrograph is included in Fig. 4(A), where it is possible to see in detail the structure of the textile threading as well as the Cu coating region, which in this case displays a largely homogeneous blue area with some random orange spots. Changes in coloring will be briefly discussed later in the paper. A red rectangle in Fig. 4(A) indicates the region where the spectra in Fig. 3 were acquired. A magnified view of that region is displayed in Fig. 4(B), which micrograph was recorded using the in-situ imaging camera that captures the green reflected light coming from the coaxial LED illumination. At the center of the region in Fig. 4(B), the irradiation experiment took place. A  $5\times 5$  matrix comprising a total of 25 ablation spots of approximately  $7\ \mu\text{m}$  in diameter was arranged as indicated in Fig. 4(C), with a lateral spacing of  $25\ \mu\text{m}$ , ensuring that all the spots reach the sample surface on a non-laser irradiated region. The high accuracy in positioning the irradiation matrix allowed recording the spectra from a selected region, in this case, a purely blue area. To carry out depth-profiling, we performed successive material ablation by repeating the irradiation of each matrix (Fig. 4(D)), progressively deepening the ablation into the

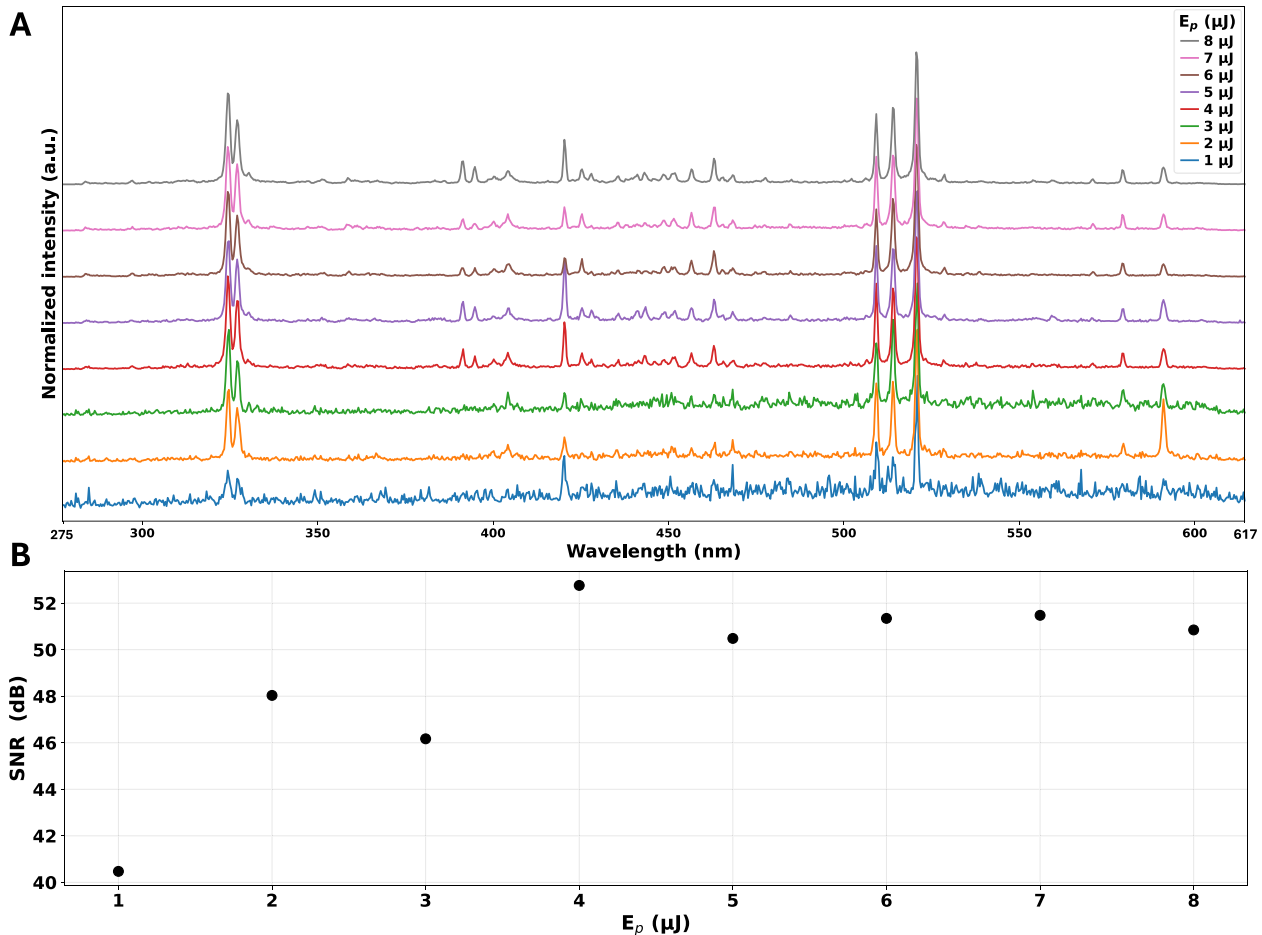


**Fig. 3** (A) Normalized intensity spectra obtained by the interaction of bandwidth-limited pulses from a Ti:Sa laser at various energy levels (1–8  $\mu\text{J}$ ) with a Cu-coated sample. (B) Plot of the signal-to-noise ratio (SNR) vs. energy per pulse ( $E_p$ ) of the spectra showed in A

sample. The focal plane of the focusing optics was fixed in the Z-direction for each matrix (M1 closer to the surface to M10 deeper in the fiber) until the acquired spectra matched those of the polymer substrate. With this procedure, the subsequent spectra analysis allowed us to determine the chemical composition of the coating in depth and enabled us to determine indirectly the coating depth by pinpointing the Cu-coating Lyocell substrate transition.

To verify that the pulse energy focused by the  $10\times$  objective was sufficient to fully ablate the Cu coating, a simulation of Gaussian beam propagation in air is presented in Fig. 5 from  $z = -100 \mu\text{m}$  (before focus) to  $z = +100 \mu\text{m}$  (after focus). The simulated laser beam had a wavelength of  $\lambda = 790 \text{ nm}$ . While the manufacturer's specification indicates  $\text{NA} = 0.28$ , in our experimental configuration, the input beam diameter at the back focal plane was  $2.83 \text{ mm}$ , and the aperture diameter was  $11.20 \text{ mm}$ , corresponding to an effective numerical aperture of  $0.071$ . The position of  $z = 0 \mu\text{m}$  corresponds to the focal plane, where the Gaussian

beam had a beam waist  $w_0 = 3.5 \mu\text{m}$  measured at  $1/e^2$ . The estimated peak fluence at the focal plane for a  $5 \mu\text{J}$  pulse energy was about  $13 \text{ J/cm}^2$ , and the focal volume at which the fluence remains above the ablation threshold is confined to a region of approximately  $48 \mu\text{m}$  around the focal plane. The colormap shows the normalized fluence on a linear scale using a false-color heatmap representation to visualize the full dynamic range. White curved lines indicate the Gaussian beam envelope.

Based on the Gaussian beam simulation (Fig. 5), the effective depth of field around the focal plane was approximately  $\pm 24 \mu\text{m}$ , corresponding to a confocal parameter of  $\sim 48 \mu\text{m}$  for the  $3.5 \mu\text{m}$  beam waist used in this work. This defines the axial region in which the fluence remains above the ablation threshold of the Cu layer. During depth-profiling measurements, repeated single-shot irradiation at a fixed Z-position progressively removes material until the focal volume intersects the underlying polymer, as evidenced by the emergence of CN and C-C emission bands.

**Fig. 4** (A) Optical profilometer micrograph of a textile sample using white light illumination showing a detailed surface structure. (B) Magnified region indicated by the red box in A, displaying the fiber surface captured with the in-situ camera. (C) Schematic of a  $5 \times 5$  ablation matrix with  $25 \mu\text{m}$  lateral spacing measured from center to center. (D) Sketch of a cross-sectional view of an iterative matrix application at fixed z-position (not to scale), enabling depth profiling from the copper oxide layer ( $\text{Cu}_2\text{O}/\text{CuO}$ ), and through multiple layers by applying successive matrices (M1, M2, ... M10) to the polymer fiber substrate

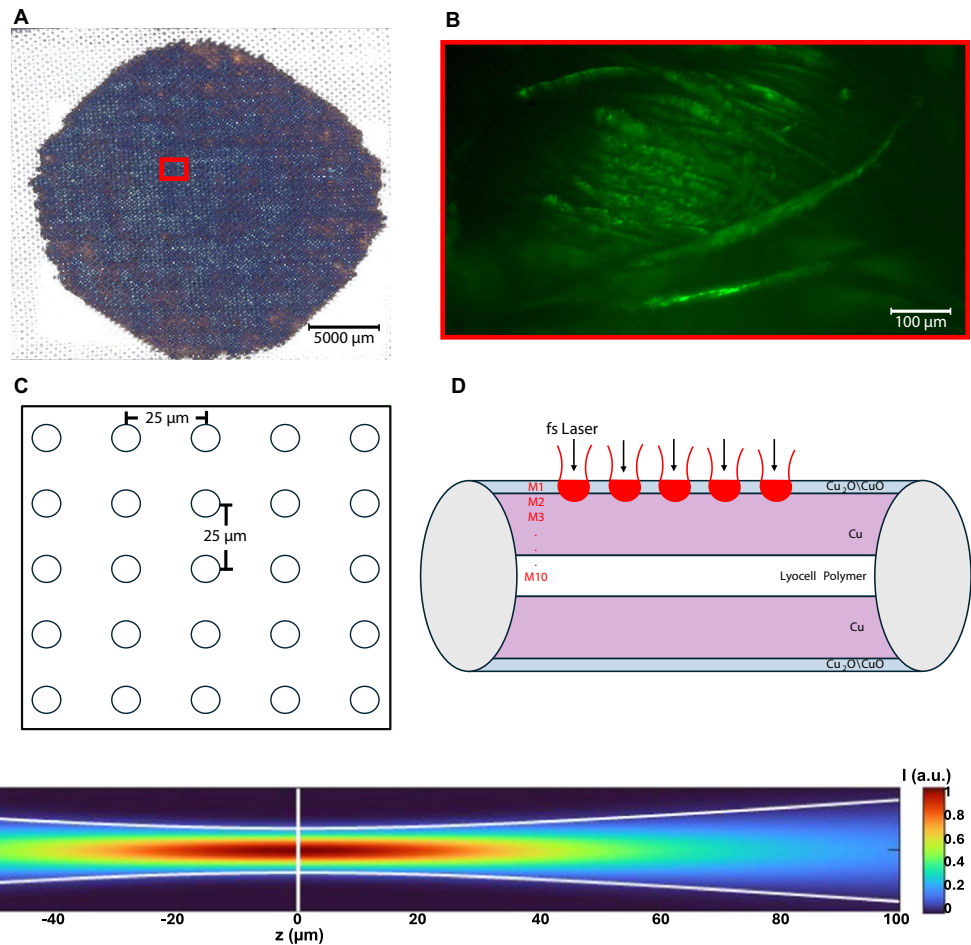


**Fig. 5** Gaussian beam propagation simulation showing the focal volume relative to the sample surface

### 3 Results and discussion

In this study, the analysis focuses on detecting and comparing relative spectral signatures associated with Cu, oxide species, and the Lyocell polymer. The objective is to identify layer transitions and coating uniformity, rather than to determine absolute elemental concentrations. All spectra were acquired under identical excitation and detection conditions to ensure that relative trends can be interpreted consistently. Absolute quantitative analysis was not pursued for two reasons. First, certified reference materials replicating the multilayer Cu/Cu<sub>2</sub>O/polymer structure are not available, making calibration against known elemental concentrations impractical. Second, the intrinsic micro-scale inhomogeneity of textile fibers prevents reproducible point-to-point quantitative calibration. For these reasons, the study is designed to capture relative spectral changes that reliably mark transitions between Cu, oxide, and polymer layers.

Although plasma temperature can influence absolute emission intensities, we note that the relative behavior of the Cu-I lines remained consistent throughout the

measurements. In the acquired spectra, the ratios of well-known Cu-I transitions at peaks 324.7 nm, 327.4 nm fluctuated only within the noise level. In addition, the ratio of emission lines between 510.5 nm, 515.3 nm, and 521.8 nm remained stable in the majority of the spectra shown in Figs. 6 and 7, indicating that the plasma temperature remained approximately constant under the fixed single-pulse excitation conditions used in this study. Therefore, the observed relative intensity changes can be attributed mainly to material transitions rather than plasma-property variations. Using identical pulse energy, focusing conditions, and detection settings for all measurements helps limit instrumental variability; however, we acknowledge that variations in sample composition may still influence plasma properties through matrix effects. Consequently, the analysis focuses on relative spectral trends and internal line-ratio consistency rather than assuming identical plasma conditions across different materials.

Given the presence of multiple trace elements introduced during the coating and preparation steps, and considering the  $\sim 1$  nm spectral resolution of the detection system, the

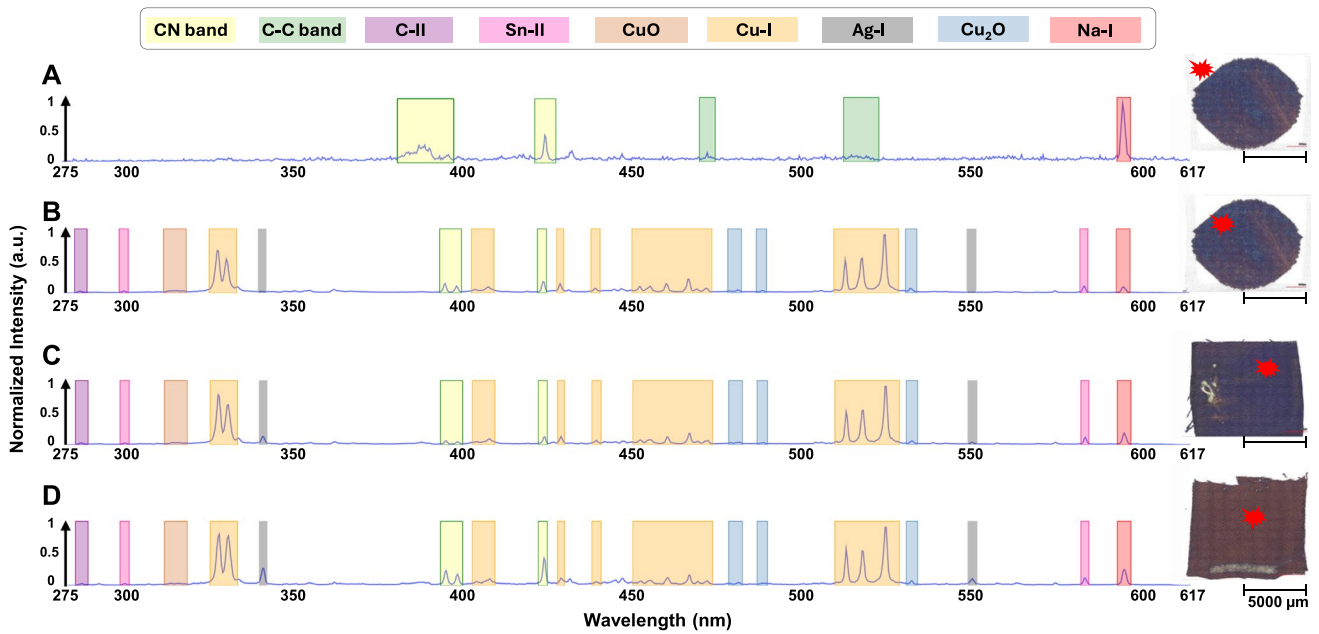


**Fig. 6** Individual normalized spectral comparison across samples showing distinct variations in chemical composition. (A) Spectra from a non-coated white region on the Lyocell substrate, revealing in particular CN and C-C bands from the polymer (B–D), spectra from coated

textiles displaying Cu peaks and oxide formations of CuO and Cu<sub>2</sub>O. Trace elements such as Ag-I, Sn-II, and Na-I appear with different concentrations across samples

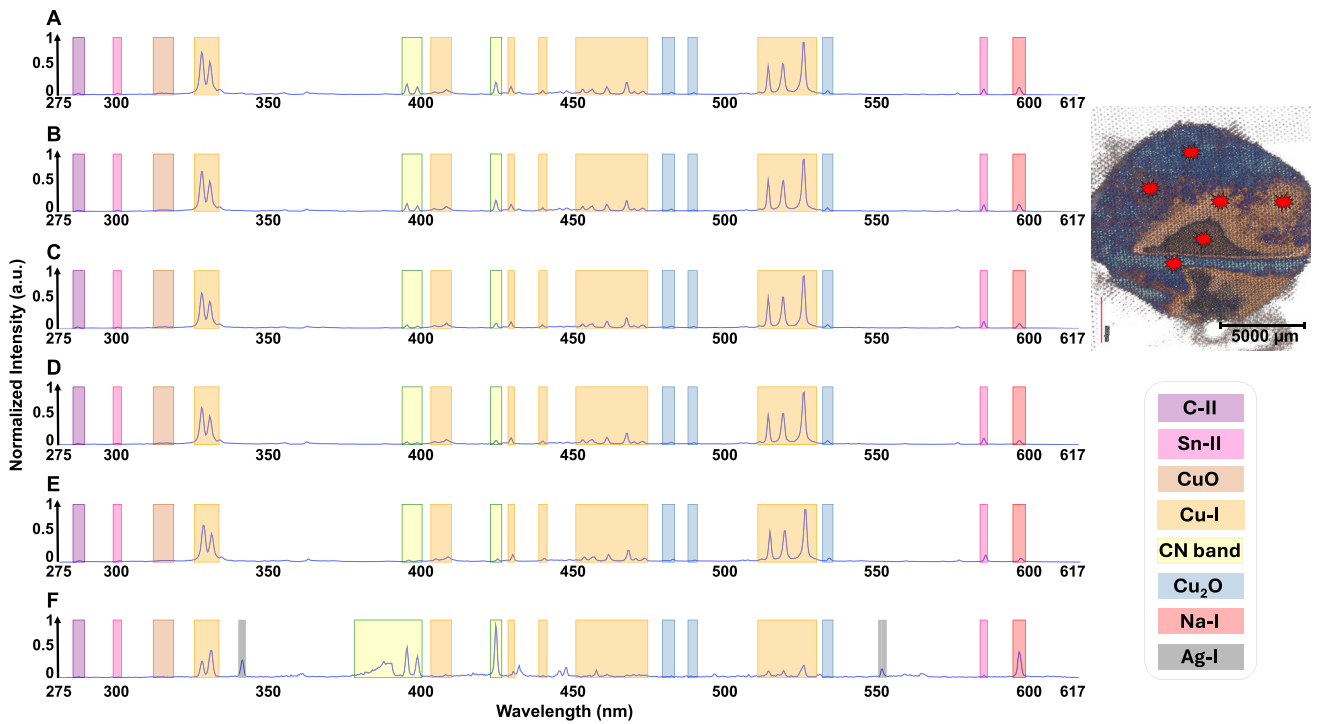


**Fig. 7** On the left, recorded spectra of mix-colored Cu-coated Lyocell fabric. The sample for this experiment is shown as an inset on the right, indicating the locations where the irradiation matrices A-F were

performed. The identified signals include C-II, Sn-II, CuO, Cu-I, CN band, Cu<sub>2</sub>O, Na-I, and Ag-I as indicated in different colors on the legend of the right

spectral interpretation focuses on well-separated and high-intensity emission lines to avoid ambiguity from potential peak overlaps. Initially, fs-LIBS analysis is conducted under the same pulse energy and focusing conditions to facilitate a comparative evaluation. Figure 6(A) illustrates the characterization of the white polymer to have baseline information about the signal from the polymer substrate. A prominent CN band is observed spanning approximately from 376 to 394 nm, with an additional distinct peak at 420 nm, both highlighted in yellow. Moreover, a C-C band extends approximately from 509 to 520 nm, accompanied by a peak at 471 nm [27–29], both highlighted in green. These bands are commonly featured in polymer analysis [21, 30], indicating the presence of the Lyocell substrate, which are typically dominant for cellulose-based materials. Additionally, an intense peak at 589 nm corresponds to the signal coming from Sodium (Na-I), highlighted in pale red. This transition is particularly intense even at trace concentrations because the Na-I D-line at 589 nm has a very high Einstein coefficient of spontaneous emission, making it easily detectable in fs-LIBS plasmas. All line assignments were cross-checked using the NIST Atomic Spectra Database [31], and only emission lines with clear separation within the available spectral resolution were considered in the analysis.

In contrast, recorded spectra plotted in Fig. 6(B–D) from Cu-coated regions, displayed a peak intensity decrease associated to the polymer substrate while increasing Cu-related peaks, including Cu-I at 324 nm, 328 nm, 400 nm, 404 nm, 424 nm, 436 nm, and a broader range of peaks centered around 460 nm, as well as three distinct peaks at 510 nm, 515 nm, and 522 nm, all highlighted in orange. On average, the intensity of these peaks remains the same on the coated samples regardless of their color. The spectra also contain peaks corresponding to Silver at 328 nm and 550 nm, (Ag-I, highlighted in grey), Tin at 299 nm and 579 nm (Sn-II, highlighted in pink), and Sodium at 589 nm (Na-I, highlighted in pale red), which were all verified against the NIST database [31], consistent with the AgNO<sub>3</sub> seeding and H<sub>2</sub>CO reduction steps, reflecting their use during the fiber coating process. It is worth mentioning here that Sn II emission appears more prominently than Sn I because tin has a lower ionization potential and its ionized transitions possess higher spontaneous emission probabilities. At the 85 ns gate delay used in this work, the plasma is in a recombining regime where weak neutral Sn I lines have already diminished, while the stronger Sn II lines remain detectable. For copper, the dominant species in the coating, the Cu I lines persist in this temporal window, whereas Cu II lines decay too rapidly to be observed. This difference explains why ionized tin –but not ionized copper– is detected under identical experimental conditions [14]. Here, the intensity of the Ag-I peaks and the CN band signal on the brownish

sample in Fig. 6(D) suggest a slightly thinner Cu-coating, as the signal from the underlying polymer is detectable –except for CN band between 376 to 394 nm– and the silver peaks are more intense. Additionally, the signal from sodium is also more intense, as presumably it comes from the polymer substrate under the coating.

Further analysis of spectra in Fig. 6(B–D) revealed the presence of cupric oxide band ranging from 312 to 318 nm (CuO, highlighted in brown) and copper oxide peaks at 478 nm, 484 nm, and 528 nm (Cu<sub>2</sub>O, highlighted in blue) [32, 33], indicating oxide formation within the Cu-coating. The fact that the spectra report only faint signals from these oxides suggests that their presence is minimal, likely due to the formation of passivation oxide layers, in which thicknesses are usually on the order of a few nanometers. The spectra showed a progressive dominance of Cu-related signals over polymer bands compared to other experiment trials.

Color changes of Cu-coated samples in Fig. 6 can be attributed to changes in the oxide coating thickness [34], due to the presence of homogeneous oxide films, or because of localized surface plasmon resonances (LSPR) produced by the interaction of light with the metallic copper nanoparticles embedded on the oxide layers. Studies using UV-vis spectroscopy and electrodynamics theory demonstrate that oxide-free Cu nanoparticles exhibit intense and narrow LSPR peaks, comparable to noble metals like Ag and Au [35]. The intensity gradient and heterogeneity in nanoparticle size and density, driven by reduction dynamics, align with research on the oxidation kinetics of copper nanocrystals, where diffusion and reaction processes affect the optical properties and stability of Cu<sub>2</sub>O nanoparticles [36].

The presence of copper oxide shells can alter plasmonic absorption, influencing both electronic properties and the observed coloration of the material [37]. Previous studies show that Cu films exhibit different colors depending on their thickness and oxidation state [23, 24, 34], with nanoparticles formed within passivation oxide layers further enhancing coloration through plasmon resonances. Optimization strategies, such as adjusting AgNO<sub>3</sub> concentration or deposition time, support these findings by enabling control over nanoparticle size and surface plasmon resonance through chemical reduction and environmental factors [38]. As shown in Fig. 1(A), specific deposition conditions produce Cu coatings with varied hues, likely arising from these plasmonic and oxidative effects. Thanks to the high spatial resolution of the proposed technique, we can precisely target regions of distinct color and use fs-LIBS to inspect potential differences in their chemical imprint.

Figure 7 displays one of the colorful samples selected from Fig. 1(A), for detailed comparison across six distinct areas (irradiation matrices displayed in Fig. 7 as A to F),

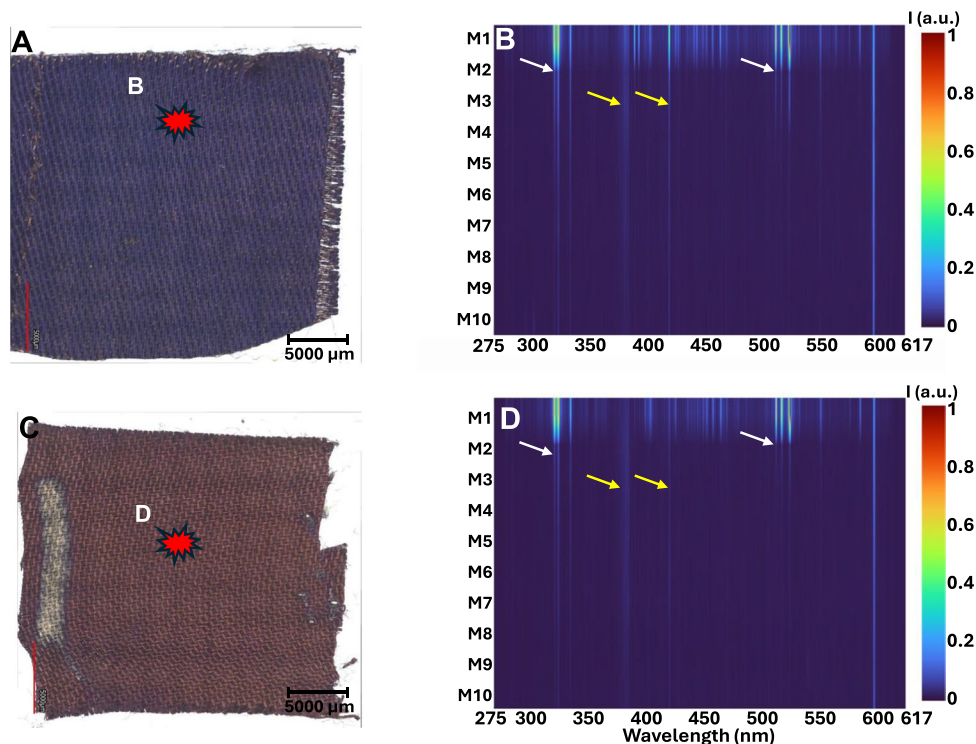
underscoring the heterogeneous coloring of the sample. The fs-LIBS spectra show Cu-related peaks (Cu-I) with rather constant signal, except in the experiment performed in Fig. 7(F), where its intensity decreases substantially. Polymer-related signals as the ones plotted in the spectra of Fig. 6(A) were prominent in Fig. 7(F), with a CN signal (highlighted in light-yellow) starting to appear clearly, in agreement with having a thinner Cu-coating compared to other samples as the brownish one displayed in Fig. 6(D). The data in the spectra is congruent with the scenario in which the coloring is mainly due to LSPR effects produced by metallic nanoparticles embedded in the oxide superficial thin film [39], and not from a different chemical composition of the film.

Faint signals corresponding to copper oxides ( $\text{Cu}_2\text{O}$  and  $\text{CuO}$ ) are detected with slight varying intensities, suggesting differences in coating thickness or oxidation levels across A-F. The rest of the highlighted detected elements (Na-I, C-II, Sn-II, Ag-I) correspond to traces from the coating fabrication process, as it was already pointed out in Fig. 6.

To obtain in-depth chemical information from the coating, trials of fs-LIBS spectra were recorded at different depths, consisting of consecutively irradiating the same area 10 times, as described in Fig. 4(D). Each matrix (M1–M10) corresponds to a single fs-LIBS shot taken at exactly the same lateral and axial position. Because the sample is not repositioned between shots, the matrices represent a sequential ablation process in which each laser pulse removes material from the same location, effectively

probing progressively deeper into the coating and substrate. No translation was applied between the consecutive shots, neither laterally nor along the z-axis. Uniformly colored samples of blue and brown color, as displayed in Figs. 8(A) and 8(C), were characterized, and the resulting spectra from the two irradiation trials were plotted using a horizontal heat map representation as displayed in Figs. 8(B) and Fig. 8(D) respectively. During the first irradiation matrix that always records information from the most external part of the coating (M1), unsurprisingly, both samples exhibited the characteristic Cu emission lines indicated by the white arrows in Fig. 8(B, D), along with the other peaks that were already shown in Fig. 7(A–E). The second matrix irradiation (M2) shows a decrease in the Cu signal on both samples, still containing the other characteristic surface peaks. Additionally, the signal from the CN band (yellow arrows in Fig. 8) starts to be detectable, suggesting that the focal volume of the laser can already ablate material under the metallic coating. Starting from the third matrix irradiation (M3), a sharp transition occurs, and the subsequent Cu signal could barely be detected at deeper matrices. For example, in Fig. 8(D), a steady attenuation of the Cu lines is recorded, combined with an increased signal from the CN polymer lines (yellow arrows). This inverse relationship between Cu and polymer emissions confirms that once the copper coating is continuously ablated, the laser focal volume rapidly reaches the polymer substrate under the coating. It is important to note that, although the focal plane remains fixed during the depth-profiling sequence, the surface recedes after each

**Fig. 8** Irradiation experiments in two homogeneously coated samples of blue and brown color as shown in (A) and (C). The spectral profiles across multiple matrix irradiation trials are presented in (B) and (D), illustrating depth profiling of the Cu layer thickness. White arrows indicate the Cu signal, whereas yellow arrows indicate the signature peaks from the polymer under the Cu-coating



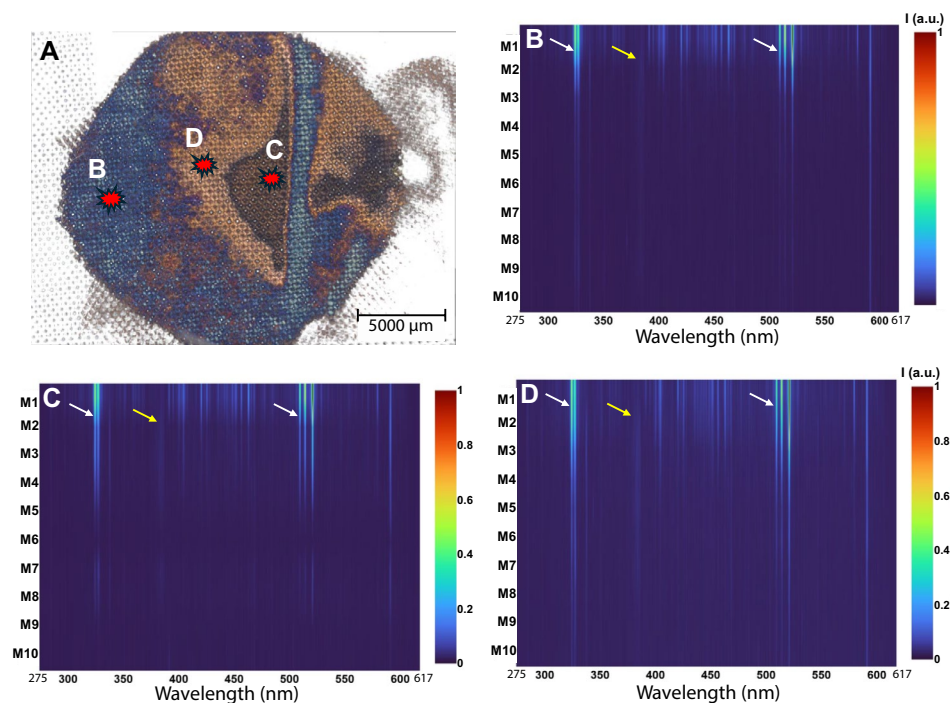
ablation pulse. As a result, the distance between the focus and the sample surface increases progressively, which can modify plasma properties such as electron temperature. Consequently, part of the decrease in emission intensity with increasing matrix number may also originate from changes in plasma excitation conditions, not only from a reduction in available Cu mass. It is important to note that, although the focal plane remains fixed during the depth-profiling sequence, the surface recedes after each ablation pulse. As a result, the distance between the focus and the sample surface increases progressively, which can modify plasma properties such as electron temperature. Consequently, part of the decrease in emission intensity with increasing matrix number may also originate from changes in plasma excitation conditions, not only from a reduction in available Cu mass. A noteworthy observation in Figs. 8(B) and 9(B,D) is the consistent Na I emission line at approximately 589 nm, which remains essentially constant throughout all depth-profiling matrices. Because sodium is homogeneously distributed within the Lyocell substrate and is exposed once the overlying Cu layer is removed, the stability of this line provides an internal reference that confirms the repeatability of the measurements and the stability of plasma conditions across successive single-shot ablations.

A similar experiment was repeated on a nonhomogeneous coating as shown in Fig. 9, with slightly higher energy of  $6 \mu\text{J}$ . Three different color positions were selected as indicated in Fig. 9(A). Across all three trial spectra in Fig. 9(B–D), the characteristic copper emission lines were strong during the first three measurement matrices M1 to M3.

Beyond M3, the Cu signal (white arrows) weakened at different rates depending on the trial. In Fig. 9(B), the Cu signal showed a rather fast decay rate, similar to the results in Fig. 8. In Fig. 9(C), signal from the Cu lines remained visible well past M3 until M5. Then, Cu peaks fade in M6 and recover intensity faintly during M7 and M8. This behavior is likely due to inhomogeneous textile coating, as the yarn is composed of different entangled fibers. This interpretation is supported by EDX analysis of a single fiber shown by yellow and white arrows in Fig. 10(C), revealing that the Cu coating is non-uniform, with regions of partial or complete substrate exposure. The CN band exhibited a similar decay trend. Its faint appearance (yellow arrows) suggests deeper Cu penetration in the laser-processed regions, indicating a gradual transition from coating to substrate. In Fig. 9(D), the decay was the slowest, detecting signal from the Cu peaks along all matrices faintly reduced by M10, along with a more prominent signal coming from the polymer, agreeing with the previously presented results. The observed spectral variations that arise might be interpreted as an intrinsic sample inhomogeneity. In particular, variations in deposition time, Ag seeding, and Cu nanoparticle distribution embedded in the oxide film led to different ablation behaviors and Cu emission intensities.

Importantly, by comparing spectra coming from samples with similar color, as the ones shown in Figs. 8(D) with 9(C), one could expect that the signals are always the same; however, they present remarkable differences, especially regarding the Cu peaks intensity. We attribute this behavior to the coating inhomogeneity of the sample shown in Fig.

**Fig. 9** fs-LIBS spectral profiles (normalized intensity) of a single Cu-coated Lyocell fabric sample across 10 matrix irradiations (M1–M10) at three color regions (B, C, D), illustrating depth profiling of Cu layer thickness with laser energy per pulse of  $6 \mu\text{J}$ . Cu peaks (marked with white arrows) decrease in intensity. Polymer peaks (e.g., CN indicated by the yellow arrow) emerge, indicating penetration through the coating



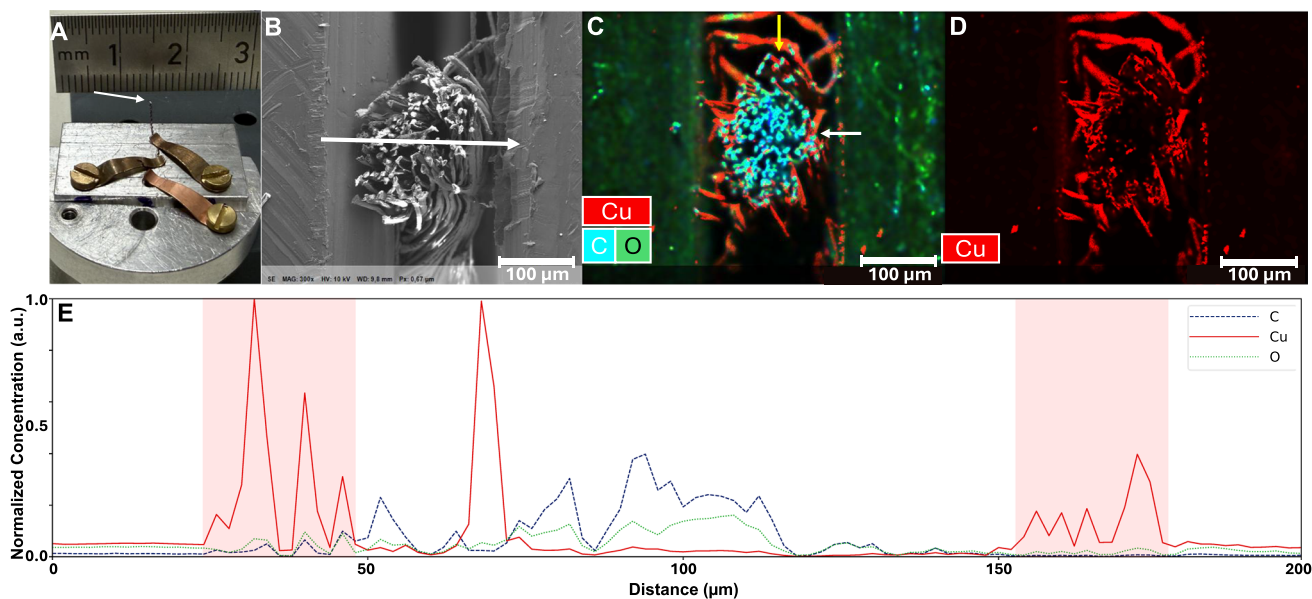


**Fig. 10** Characterization of a Cu-coated Lyocell fiber. **(A)** Extraction and mounting of a single fiber. **(B)** SEM cross-section image. **(C)** EDX elemental map showing Cu, C, and O distributions. **(D)** Cu-only map

highlighting coating homogeneity. **(E)** Line-scan elemental profile along the arrow in **(B)**. Shaded regions mark Cu-rich coating zones

9(A), caused by extended deposition (up to 2 hours) and varying Ag seeding. This leads to a non-uniform Cu-coating and Cu nanoparticles spread on Lyocell fibers. While Ag seeds catalyze Cu reduction, higher concentrations or prolonged deposition can cause aggregation or uneven bath penetration, resulting in micro-scale variations in Cu thickness, nanoparticle, and oxides formation ( $\text{Cu}_2\text{O}/\text{CuO}$ ). In uniform samples, shorter deposition times produce consistent Cu oxides ratios, yielding stable Cu line intensities. In contrast, the inhomogeneous sample in Fig. 9 may have local domains with thinner oxides, denser Cu nanoparticles, or mixed phases. At the same time, the shown data highlights the capability of fs-LIBS to detect such variations, as the technique readily distinguishes color regions within a single specimen and accurately tracks the remaining Cu layer depth at each position, demonstrating both high sensitivity and good measurement stability.

The thickness of the Cu coating on an individual Lyocell fiber was indirectly estimated using EDX combined with scanning electron microscopy (SEM). A single coated fiber extracted from a blue-colored region of Fig. 1 was separated from the thread bundle and mounted transversely as shown in Fig. 10(A). After cutting the fiber to expose its cross-section, an SEM micrograph was recorded (Fig. 10(B)), and EDX mapping was performed along the indicated white arrow. The resulting elemental distribution maps are shown in Fig. 10(C–D). Copper (red), carbon (cyan), and oxygen (green) appear in false colors, and the orange regions visible in Fig. 10(C) originate from the overlap between the Cu and C signals, highlighting areas where the coating partially

penetrates into the fiber surface. The white and yellow arrows in Fig. 10(C–D) indicate local variations in coating thickness and regions where the Cu layer becomes discontinuous. Displaying only the Cu signal, as in Fig. 10(D), further emphasizes these inhomogeneities.

An elemental line profile extracted along the white arrow in Fig. 10(B) is shown in Fig. 10(E). The shaded pink regions correspond to Cu-rich zones of approximately 20 μm thickness located at both sides of the 200 μm fiber diameter. This profile confirms that the Cu coating forms a continuous shell around the fiber circumference. These EDX observations are consistent with the fs-LIBS depth-profiling results, which showed a gradual transition from the Cu layer to the underlying polymer substrate and required multiple pulses to fully remove the metallic coating depending on local coating thickness.

## 4 Conclusion

Femtosecond laser-induced breakdown spectroscopy is used in this study as an efficient and precise approach for analyzing Cu-coated Lyocell fabrics of homogeneous and heterogeneous coloring. The focused laser pulses provided a minimum area attained to the laser beam diameter of 7 μm at the focal plane, allowing for single-out specific colored domains with true micrometric lateral resolution. Axially, the implemented beam allows characterizing coatings which maximum thickness could range the confocal parameter of the used optics, in this case ~100 μm. The measured

thickness of the Cu coating in this case was approximately 20  $\mu\text{m}$ . This is confirmed by cross-sectional SEM images and EDX line scans that allow identifying spatially the Cu concentration. All interpretations rely on relative spectral behaviors rather than absolute elemental concentrations, as the study is designed for detection and depth-resolved characterization rather than quantitative compositional analysis. This detection-oriented approach is consistent with the scope of fs-LIBS for resolving layer transitions and identifying chemical signatures in heat-sensitive multilayer structures.

The technique successfully identifies elemental compositions, including Cu-I, and trace elements such as Sn-II and Na-I, while detecting faint CuO and Cu<sub>2</sub>O signals that correlate with observed color variations. By enabling depth profiling, we get insights into the coating depth of the various colored regions and investigate their transitions to the underlying polymer substrate. We conclude that fs laser pulses facilitate the detection of signals originating from the heat-sensitive polymer substrate beneath the metallic coating, as well as dielectric intensity peaks associated with oxides present within the coating layer. The homogeneity of the copper-coating is a critical parameter for reliable in-depth characterization, as variations in oxidation levels and in the concentration of nanoparticles within the oxide films can influence the measurements. In the case of textile samples exhibiting uniform Cu coatings, the in-depth Cu signal remains consistent across different sample colors. Conversely, when the Cu coating is non-uniform such as in samples produced with varying deposition times, marked differences are observed in both the optical appearance and the corresponding in-depth fs-LIBS profiles. We demonstrated that the technique is able to analyze heat-sensitive substrates, making it an efficient tool for quality assurance in textile-based flexible electronics. These results highlight the potential of fs-LIBS, particularly in the context of dielectric materials, stemming from its ability to provide precise, high-resolution analysis while minimizing thermal effects and enhancing signal quality, which is crucial in advancing the development of smart textiles and flexible electronics, where precise characterization of metallic coatings is critical for ensuring performance and durability. The ability to detect microscale variations and oxide formations provides valuable insights into coating processes, supporting optimization strategies such as adjusting deposition times or seeding concentrations. The stability of the Cu-I line ratios confirms that plasma-related variations did not dominate the observed trends. Likewise, the constant Na-I emission across all matrices further demonstrates the repeatability of the measurements and supports the reliability of the relative intensity changes observed during depth profiling. Future research could explore fs-LIBS applicability to quantify other metallic coatings and substrates, further establishing

its role in real-time monitoring and quality control for next-generation wearable devices, energy harvesting systems, and the manufacturing of flexible batteries.

**Acknowledgements** This work was partially supported by the Bit-Werk project "Biologische Transformation technischer Werkstoffe", the Pilot-ZFF project "Laser-assisted complex materials deposition using temporally and spatially shaped ultrashort laser pulses", and the ZLF project "Learning how to measure light" funded by Kassel University.

**Author Contributions** Omar Elsheikh: Writing — original draft preparation; Writing — review and editing; Data curation; Methodology; Formal analysis and investigation; Bastian Zielinski: Writing — review and editing; Methodology. Noemí Aguiló-Aguayo: Writing — review and editing; Resources. Elena Ramela Ciobotea, Cristian Sarpe, Hendrike Braun, Arne Senftleben: Methodology; Thomas Baumert: Funding acquisition; Resources; Review and Editing. Camilo Florian: Writing — review and editing; Methodology; Conceptualization; Formal analysis and investigation; Funding acquisition; Resources; Supervision; Validation. All the authors contributed to the revision of the paper.

**Funding** Open Access funding enabled and organized by Projekt DEAL. This work was partially supported by the BitWerk project "Biologische Transformation technischer Werkstoffe", the Pilot-ZFF project "Laser-assisted complex materials deposition using temporally and spatially shaped ultrashort laser pulses", and the ZLF project "Learning how to measure light" funded by Kassel University.

**Data Availability** The data that support the findings of this study are available from the corresponding author upon reasonable request.

## Declarations

**Conflicts of Interest** The authors has no conflict of interest.

**Open Access** This article is licensed under a Creative Commons Attribution 4.0 International License, which permits use, sharing, adaptation, distribution and reproduction in any medium or format, as long as you give appropriate credit to the original author(s) and the source, provide a link to the Creative Commons licence, and indicate if changes were made. The images or other third party material in this article are included in the article's Creative Commons licence, unless indicated otherwise in a credit line to the material. If material is not included in the article's Creative Commons licence and your intended use is not permitted by statutory regulation or exceeds the permitted use, you will need to obtain permission directly from the copyright holder. To view a copy of this licence, visit <http://creativecommons.org/licenses/by/4.0/>.

## References

1. A. Kamyshny, S. Magdassi, Conductive nanomaterials for 2D and 3D printed flexible electronics. *Chem. Soc. Rev.* **48**(6), 1712–1740 (2019). <https://doi.org/10.1039/C8CS00738A>
2. C. Wang, K. Xia, H. Wang, X. Liang, Z. Yin, Y. Zhang, Advanced Carbon for Flexible and Wearable Electronics. *Adv. Mater.* **31**(9), 1801072 (2019). <https://doi.org/10.1002/adma.201801072>

3. H. Wu, Y. Huang, F. Xu, Y. Duan, Z. Yin, Energy Harvesters for Wearable and Stretchable Electronics: From Flexibility to Stretchability. *Adv. Mater.* **28**(45), 9881–9919 (2016). <https://doi.org/10.1002/adma.201602251>
4. C. Guo, Functional Materials for Flexible Electronics and Smart Wearables: Advances and Applications. *ACE* **147**, 142–150 (2025). <https://doi.org/10.54254/2755-2721/2025.22616>
5. D.A. Cremers, L.J. Radziemski, *Handbook of Laser-Induced Breakdown Spectroscopy* (2013). <https://doi.org/10.1002/9781118567371>
6. C. Lv, N. Zhang, Z. Lin, T. Ou, J. Li, N. Zhao, X. Yang, Q. Ma, L. Guo, Q. Zhang, Determination of copper, magnesium, and manganese in aluminum alloys using laser-induced breakdown spectroscopy based on fiber laser ablation. *J. Laser Appl.* **35**(1), 012021 (2023). <https://doi.org/10.2351/7.0000939>
7. J. Mildner, C. Sarpe, N. Goette, D. Otto, M. Wollenhaupt, T. Baumert, W. Wessel, E. Merdian, A. Brueckner-Foit, Optimization of the LIBS signal for the chemical mapping of metals by femtosecond double-pulses; Optimierung des LIBS-Signals zur chemischen Abbildung von Metallen durch Femtosekunden Doppelpulse. *Verh. Dtsch. Phys. Ges.* (2011). <https://www.osti.gov/etdeweb/biblio/22030754>
8. J.A. Aguilera, C. Aragón, F. Peñalba, Plasma shielding effect in laser ablation of metallic samples and its influence on LIBS analysis. *Appl. Surf. Sci.* **127–129**, 309–314 (1998). [https://doi.org/10.1016/S0169-4332\(97\)00648-X](https://doi.org/10.1016/S0169-4332(97)00648-X)
9. W. Berthou, M. Legallais, B. Bousquet, V. Motto-Ros, F. Le Cras, Characterization of lithium phosphorus oxide thin film libraries by laser-induced breakdown spectroscopy imaging: A step towards high-throughput quantitative analyses. *Spectrochim. Acta, Part B* **215**, 106906 (2024). doi: 10.1016/j.sab.2024.106906
10. B. Le Bellego, V. Motto-Ros, B. Luais, C. Fabre, C. Dalou, P. Condamine, L. Tissandier, Semi-quantitative  $\mu$ LIBS mapping of germanium diffusion between metal and silicate during planetary core–mantle segregation. *Spectrochim. Acta, Part B* **222**, 107059 (2024). doi: 10.1016/j.sab.2024.107059
11. A. Assion, M. Wollenhaupt, L. Haag, F. Mayorov, C. Sarpe-Tudoran, M. Winter, U. Kutschera, T. Baumert, Femtosecond laser-induced-breakdown spectrometry for Ca<sup>2+</sup> analysis of biological samples with high spatial resolution. *Appl. Phys. B* **77**(4), 391–397 (2003). <https://doi.org/10.1007/s00340-003-1262-z>
12. E.R. Ciobotea, C. Sarpe, B. Zielinski, H. Braun, A. Senftleben, S. Dutta, G. Mayer, C. Florian, T. Baumert, Signal enhancement with double-pulse LIBS on biological samples and better discrimination of tissues through machine learning algorithms. *Spectrochim. Acta, Part B* **222**, 107063 (2024). doi: 10.1016/j.sab.2024.107063
13. W. Wessel, A. Brueckner-Foit, J. Mildner, L. Englert, L. Haag, A. Horn, M. Wollenhaupt, T. Baumert, Use of femtosecond laser-induced breakdown spectroscopy (fs-LIBS) for micro-crack analysis on the surface. *Eng. Fract. Mech.* **77**(11), 1874–1883 (2010). <https://doi.org/10.1016/j.engfracmech.2010.03.020>
14. T.A. Labutin, V.N. Lednev, A.A. Ilyin, A.M. Popov, Femtosecond laser-induced breakdown spectroscopy. *J. Anal. At. Spectrom.* **31**(1), 90–118 (2015). <https://doi.org/10.1039/C5JA00301F>
15. E.L. Gurevich, R. Hergenröder, Femtosecond Laser-Induced Breakdown Spectroscopy: Physics, Applications, and Perspectives. *Appl. Spectrosc.* **61**(10), 233A–242A (2007). <https://doi.org/10.1366/000370207782217824>
16. C.M. Ahamer, K.M. Riepl, N. Huber, J.D. Pedarnig, Femtosecond laser-induced breakdown spectroscopy: Elemental imaging of thin films with high spatial resolution. *Spectrochim. Acta, Part B* **136**, 56–65 (2017). <https://doi.org/10.1016/j.sab.2017.08.005>
17. N. Giannakaris, A. Haider, C.M. Ahamer, S. Grünberger, S. Trautner, J.D. Pedarnig, Femtosecond Single-Pulse and Orthogonal Double-Pulse Laser-Induced Breakdown Spectroscopy (LIBS): Femtogram Mass Detection and Chemical Imaging with Micrometer Spatial Resolution. *Appl. Spectrosc.* **76**(8), 926–936 (2021). <https://doi.org/10.1177/00037028211042398>
18. S. Sheta, M.S. Afgan, L. Jiacen, W. Gu, Z. Hou, Z. Wang, Insights into Enhanced Repeatability of Femtosecond Laser-Induced Plasmas. *ACS Omega* **5**(47), 30425–30435 (2020). <https://doi.org/10.1021/acsomega.0c03636>
19. S. Saha, J. Sanwal, P. Mahadik, P. Sengupta, P. Mathi, The analytical potential of Femtosecond Laser-Induced Breakdown Spectroscopy (fsLIBS) for determination of trace elements in speleothems. *Microchem. J.* **207**, 112215 (2024). <https://doi.org/10.1016/j.microc.2024.112215>
20. R. Garcia, F.A. Stevie, L. Giannuzzi, FIB Sample Preparation for In Depth EDS Analysis. *Microsc. Microanal.* **25**(S2), 914–915 (2019). <https://doi.org/10.1017/S1431927619005300>
21. J. Kovač, M. Finšgar, Analysis of the Thermal Stability of Very Thin Surface Layers of Corrosion Inhibitors by Time-of-Flight Secondary Ion Mass Spectrometry. *J. Am. Soc. Mass Spectrom.* **29**(12), 2305–2316 (2018). <https://doi.org/10.1007/s13361-018-2048-1>
22. G. Stelmacovich, L. van Eijk, M. Walker, D.A. Cullen, S. Ware, J.L. Young, G. Bender, S. Pylypenko, Optimization of Time-of-Flight Secondary Ion Mass Spectrometry for Analysis of Porous Transport Layers. *Meet. Abstr. MA2023-01*(36), 1964 (2023). doi: 10.1149/MA2023-01361964mtgabs
23. J. Landsiedel, J. Tschannett, M. Lenninger, S. Stroj, M. Domke, T. Bechtold, T. Pham, N. Aguiló-Aguayo, A siloxane interlayer approach to enhance surface metallization on polyamide fabrics via electroless copper deposition. *Surf. Interfaces* **42**, 103434 (2023). <https://doi.org/10.1016/j.surfint.2023.103434>
24. J. Landsiedel, W. Root, C. Schramm, A. Menzel, S. Witzleben, T. Bechtold, T. Pham, Tunable colors and conductivity by electroless growth of Cu/Cu<sub>2</sub>O particles on sol-gel modified cellulose. *Nano Res.* **13**(10), 2658–2664 (2020). <https://doi.org/10.1007/s12274-020-2907-5>
25. H. Zhao, L. Hou, S. Bi, Y. Lu, Enhanced X-Band Electromagnetic-Interference Shielding Performance of Layer-Structured Fabric-Supported Polyaniline/Cobalt–Nickel Coatings. *ACS Appl. Mater. Interfaces.* **9**(38), 33059–33070 (2017). <https://doi.org/10.1021/acsaami.7b07941>
26. J. Köhler, M. Wollenhaupt, T. Bayer, C. Sarpe, T. Baumert, Zep-tosecond precision pulse shaping. *Opt. Express* **19**(12), 11638–11653 (2011)
27. T.A. Alrebbi, A. Fayyaz, A. Ben Gouider Trabelsi, H. Asghar, F.H. Alkallas, A.M. Alshehri, Vibrational Emission Study of the CN and C<sub>2</sub> in Nylon and ZnO/Nylon Polymer Using Laser-Induced Breakdown Spectroscopy (LIBS). *Polymers* **14**(17), 3686 (2022). doi: 10.3390/polym14173686
28. I. Chamradová, P. Pořízka, J. Kaiser, Laser-Induced Breakdown Spectroscopy analysis of polymers in three different atmospheres. *Polym. Test.* **96**, 107079 (2021). <https://doi.org/10.1016/j.polymertesting.2021.107079>
29. Z. Gajarska, L. Brunnbauer, H. Lohninger, A. Limbeck, Identification of 20 polymer types by means of laser-induced breakdown spectroscopy (LIBS) and chemometrics. *Anal. Bioanal. Chem.* **413**(26), 6581–6594 (2021). <https://doi.org/10.1007/s00216-021-03622-y>
30. H.L. Xu, J. Bernhardt, P. Mathieu, G. Roy, S.L. Chin, Understanding the advantage of remote femtosecond laser-induced breakdown spectroscopy of metallic targets. *J. Appl. Phys.* **101**(3), 033124 (2007). <https://doi.org/10.1063/1.2437580>
31. N.I. of Standards, Technology, Security requirements for cryptographic modules. *Tech. Rep. Federal Information Processing Standards Publications (FIPS) 140–2*, Change Notice 2 December 03, 2002, U.S. Department of Commerce, Washington, D.C. (2001). doi: 10.6028/nist.fips.140-2

32. N. Hussain, M.A. Abdelkareem, H. Alawadhi, A.H. Alami, K. Elsaid, Cu<sub>2</sub>O nanoparticles decorated with MoS<sub>2</sub> sheets for electrochemical reduction of CO<sub>2</sub> with enhanced efficiency. *Appl. Phys. A* **128**(2), 1–11 (2022). <https://doi.org/10.1007/s00339-021-05230-0>
33. L.C. Chen, C.C. Chen, K.C. Liang, S.H. Chang, Z.L. Tseng, S.C. Yeh, C.T. Chen, W.T. Wu, C.G. Wu, Nano-structured CuO-Cu<sub>2</sub>O Complex Thin Film for Application in CH<sub>3</sub>NH<sub>3</sub>PbI<sub>3</sub> Perovskite Solar Cells. *Nanoscale Res. Lett.* **11**(1), 1–7 (2016). <https://doi.org/10.1186/s11671-016-1621-4>
34. S.J. Kim, S. Kim, J. Lee, Y. Jo, Y.S. Seo, M. Lee, Y. Lee, C.R. Cho, J.p. Kim, M. Cheon, J. Hwang, Y.I. Kim, Y.H. Kim, Y.M. Kim, A. Soon, M. Choi, W.S. Choi, S.Y. Jeong, Y.H. Lee, Color of Copper/Copper Oxide. *Adv. Mater.* **33**(15), 2007345 (2021). doi: 10.1002/adma.202007345
35. G.H. Chan, J. Zhao, E.M. Hicks, G.C. Schatz, R.P. Van Duyne, Plasmonic Properties of Copper Nanoparticles Fabricated by Nanosphere Lithography. *Nano Lett.* **7**(7), 1947–1952 (2007). <https://doi.org/10.1021/nl070648a>
36. K.P. Rice, A.S. Paterson, M.P. Stoykovich, Nanoscale Kirkendall Effect and Oxidation Kinetics in Copper Nanocrystals Characterized by Real-Time, In Situ Optical Spectroscopy. *Part. Part. Syst. Char.* **32**(3), 373–380 (2015). <https://doi.org/10.1002/ppsc.201400155>
37. S.F. Bartolucci, A.C. Leff, J.A. Maurer, Gold–copper oxide core–shell plasmonic nanoparticles: the effect of pH on shell stability and mechanistic insights into shell formation. *Nanoscale Adv.* **6**(9), 2499–2507 (2024). <https://doi.org/10.1039/D3NA01000G>
38. T.M.D. Dang, T.T.T. Le, E. Fribourg-Blanc, M.C. Dang, Synthesis and optical properties of copper nanoparticles prepared by a chemical reduction method. *Adv. Nat. Sci.: Nanosci. Nanotechnol.* **2**(1), 015009 (2011). doi: 10.1088/2043-6262/2/1/015009
39. M.S. Rodrigues, J. Borges, C. Lopes, R.M.S. Pereira, M.I. Vasilevskiy, F. Vaz, Gas Sensors Based on Localized Surface Plasmon Resonances: Synthesis of Oxide Films with Embedded Metal Nanoparticles, Theory and Simulation, and Sensitivity Enhancement Strategies. *Appl. Sci.* **11**(12), 5388 (2021). <https://doi.org/10.3390/app11125388>

**Publisher's Note** Springer Nature remains neutral with regard to jurisdictional claims in published maps and institutional affiliations.